Effects of interfacial energy on compaction creep by intergranular pressure solution: Theory versus experiments on a rock analog (NaNO₃)

H. J. M. Visser,[1,2] C. J. Spiers,[1] and S. J. T. Hangx[1,3]

[1] Pressure solution plays an important role in compaction and lithification of sediments and fault gouges, but the effects of interfacial energy on this process are generally neglected. Here, microphysical models for densification of solid/liquid systems by pressure solution are derived, accounting for interfacial energy besides stress-related driving forces. They predict that densification by pressure solution creep will slow down at very fine grain sizes, where opposing interfacial energy driving forces become important compared to applied stress, and will come to a halt below a certain "yield" stress. To test the models, uniaxial compaction creep experiments were performed at ambient conditions on granular NaNO₃ aggregates (d = 8–250 μm, σ_{eff} = 0.0062–4.9 MPa). Though no significant creep occurred in dry or oil-flooded material, rapid, grain-size sensitive creep occurred in the presence of saturated NaNO₃ solution. At high effective stresses (σ_{eff} > 0.025 MPa), wet-compacted, coarser-grained (d > 20 μm) samples showed compaction behavior roughly consistent with diffusion-controlled pressure solution involving negligible interfacial energy effects. Creep rates in this regime imply an effective grain boundary diffusivity product of 5.7 × 10^{-19} m³/s. At low effective stress (σ_{eff} < 0.025 MPa), finer-grained samples (d < 20 μm) showed a decrease in strain rate with decreasing grain size, reflecting a growing influence of interfacial energy-related driving forces. This demonstrates a yield stress effect, broadly consistent with the predictions of the models incorporating interfacial energy and imply that compaction by pressure solution can be strongly inhibited in very fine-grained materials, such as nanogouge in seismogenic faults.

Citation: Visser, H. J. M., C. J. Spiers, and S. J. T. Hangx (2012), Effects of interfacial energy on compaction creep by intergranular pressure solution: Theory versus experiments on a rock analog (NaNO₃), *J. Geophys. Res.*, *117*, B11211, doi:10.1029/2012JB009590.

1. Introduction

[2] Pressure solution creep is known to be important in fluid-rock aggregates under relatively low stresses where dislocation creep is slow [*den Brok et al.*, 1999; *Lehner and Bataille*, 1984; *Lehner*, 1990; *Pharr and Ashby*, 1983; *Raj*, 1982; *Robin*, 1978; *Rutter*, 1976; *Spiers and Schutjens*, 1990; *Spiers et al.*, 2004; *Watson and Brenan*, 1987]. Since pressure solution processes are accelerated in fine-grained materials [*de Meer and Spiers*, 1997; *Zhang and Spiers*, 2005; *Zhang et al.*, 2010], they are of particular interest in relation to the compaction, healing/sealing and restrengthening of fault gouges [*Bos and Spiers*, 2001, 2002; *Dewhurst and Jones*, 2002; *Elsworth and Yasuhara*, 2006; *Morrow and Byerlee*, 1989; *Niemeijer et al.*, 2008, 2010], notably in the seismogenic zone of major fault systems. Compaction of porous rock systems by pressure solution occurs due to an increase in solubility at grain-to-grain contacts under stress, compared with pore-wall regions. This drives material transport from contacts to pores, resulting in compaction of the aggregate and porosity/permeability reduction.

[3] Compaction by pressure solution has been extensively studied both theoretically and experimentally [e.g., *de Meer and Spiers*, 1995; *Gratier et al.*, 2009; *Green*, 1984; *Lehner*, 1990; *Raj and Chyung*, 1981; *Renard et al.*, 1999; *Rutter*, 1976; *Spiers and Schutjens*, 1990; *Spiers et al.*, 1990; *Zhang et al.*, 2002]. However, though the intergranular stresses assumed in most theoretical treatments, and applied in many experimental studies, were generally low, the effects of interfacial energy were disregarded or assumed to be negligible. In contrast, other studies of fluid-rock systems have solely considered the effects of interfacial energy in

[1] High Pressure and Temperature Laboratory, Department of Geosciences, Utrecht University, Utrecht, Netherlands.
[2] Now at Energy Research Centre of the Netherlands, Petten, Netherlands.
[3] Now at Shell Global Solutions International, Rijswijk, Netherlands.

Corresponding author: S. J. T. Hangx, Shell Global Solutions International, Kesslerpark 1, NE 2288 GS Rijswijk, Netherlands. (suzanne.hangx@shell.com)
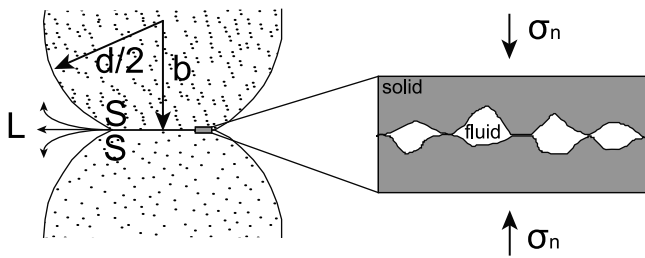
Figure 1. Schematic diagram of a grain contact undergoing pressure solution creep with mass transfer through an island channel type grain-to-grain contact (see inset). Note that σ_n is the normal stress to the contact, d is the grain size, b is the distance from the grain center to the contact, and S and L stand for solid and liquid, respectively.

bringing about processes such as neck growth at grain contacts to achieve equilibrium dihedral contact angles [*Bulau et al.*, 1979; *Faul*, 1997; *Hay and Evans*, 1988; *Hickman and Evans*, 1991; *Jurewicz and Watson*, 1985], or else processes such as grain growth [*Evans et al.*, 2001; *Olgaard and Evans*, 1988]. Only a few studies have considered both interfacial energy and differential stress as competing driving forces for material transport and porosity/permeability change in fluid-bearing aggregates [*Coble*, 1967, 1970; *German*, 1985; *Heidug*, 1991; *Spiers and Schutjens*, 1999; *van Noort et al.*, 2008a; *Visser*, 1999], despite clear experimental evidence that both can be important (e.g., compare *Hickman and Evans* [1991], *Spiers and Schutjens* [1999], and *Visser* [1999]).

[4] In this paper, microphysical models for densification and microstructural changes of granular solid/liquid systems by pressure solution creep are extended, to account for both interfacial energy and effective stress as driving forces for material transport. The new models are then experimentally tested using a simple, two-component rock analog system, namely NaNO$_3$ plus saturated solution at ambient conditions. One-dimensional compaction experiments were performed, in which the applied stress and grain size were varied systematically. In this way, the dependence of strain rate on stress and grain size could be determined and compared with the extended microphysical models. In particular, these experiments were performed with the aim of investigating the occurrence of a possible "yield stress" for pressure solution creep, caused by interfacial energy forces opposing the effect of applied effective stress [see *Revil*, 2001; *Revil et al.*, 2006; *van Noort et al.*, 2008b; *Visser*, 1999].

2. Microphysical Model for Compaction of Solid/Liquid Systems Under Stress

2.1. Background on Compaction by Pressure Solution Creep

[5] We begin by outlining an idealized theoretical framework for the treatment of pressure solution. In so doing, we consider an aggregate of identical spherical grains of a homogeneous and isotropic solid substance, its pore space being saturated by an aqueous solution of the solid component. Grain contacts are assumed to be flat, as represented in the two-grain model in Figure 1. In general, the system sustains some macroscopic state of stress and a (uniform)

pore fluid pressure P_f. The solution will be in chemical equilibrium with the solid, locally at any point along the free pore walls, if the chemical potential of the solute μ_S equals the local "equilibrium chemical potential" μ_{eq} at that point, that is, if it satisfies the condition [*Gibbs*, 1878, equation (661)]

$$\mu_s = \mu_{eq} = f^s + P_f V_{m,s} + \gamma\left(\frac{1}{r_1} + \frac{1}{r_2}\right)V_{m,s} \quad (1)$$

Here, f^s is the molar free energy of the solid and $V_{m,s}$ is its molar volume, γ is the interfacial energy (in J/m^2) between the solid and the liquid, and r_1 and r_2 are the principle radii of interfacial curvature (positive when their centers lie on the same side of the interface). Note that μ_{eq} is a quantity defined in the solid phase that depends on the state of stress in the solid, through f^s and $V_{m,s}$, and, in general, will vary from point to point along the solid/fluid interface. When a granular solid plus intergranular liquid system of this type is loaded isostatically, such that the solid framework of spherical grains supports a positive effective stress, the grain contacts will support a total normal stress σ_n (see Figure 1), while pore walls experience the fluid pressure P_f. Following *Lehner* [1990], to evaluate the solid potential within loaded grain contacts, we employ the concept of a grain-to-grain contact zone and consider a representative, pillbox shaped element (Figure 1). Regardless of the fluid-permeated grain boundary structure within it, one may then consider normal tractions and other properties of the solid phase along the boundaries of such an element, and from these define a local chemical potential of the solid, that is, the normal component of the chemical potential tensor [*Lehner*, 1995]. This is given by

$$\mu_{gb} \approx f^s + \sigma_n V_{m,s} \quad (2)$$

where all quantities are to be interpreted as averages taken over surface elements of the size of the representative pill box. The potential μ_{gb} is thus a "local" property of the solid phase along a nominally flat grain-to-grain contact (see Figure 1, and for more detail details, see *Lehner and Bataille* [1984], *Lehner* [1990, 1995], and *Spiers and Schutjens* [1990]).

[6] Provided that grain contacts are penetrated by a fluid phase in thin film or island-channel form and that the stress supported by the solid framework is sufficiently high for the potential difference between solid sites along the grain contact and the solute component in the (well-mixed) open pore fluid to become positive, that is, $\mu_{gb} - \mu_s > 0$, intergranular pressure solution, accompanied by aggregate densification, can occur. Assuming there is no long-range diffusive or advective transport in or out of the system (i.e., assuming a chemically closed system), and disregarding any minor loss of mass of the solid component resulting from the expulsion of the solution phase during compaction, the pressure solution process can be regarded as a succession of steady states in which the overall rates of dissolution and precipitation balance, and where the rate of compaction is controlled by the kinetics of the three serial steps of dissolution, diffusion, and precipitation [*de Meer and Spiers*, 1997; *Lehner*, 1990, 1995; *Raj*, 1982]. The kinetics of creep can hence be specified in terms of crystal growth/dissolution laws or Ficks law for diffusion. The local

driving force for this process is given by $\Delta\mu = \mu_{gb} - \mu_{eq}$, where it is classically assumed that variations in f^s and $V_{m,s}$ between contacts and pores as well as interfacial energy effects can be neglected [de Meer and Spiers, 1997; Lehner, 1995; Spiers et al., 2004].

[7] Constitutive models for compaction by intergranular pressure solution taking diffusion as the rate-controlling step have been developed by numerous authors [e.g., Gratier et al., 2009; Gundersen et al., 2002; Lehner, 1990; Niemeijer et al., 2002; Raj, 1982; Renard et al., 1999; Rutter, 1976; Spiers et al., 1990; Spiers and Brzesowsky, 1993; Spiers et al., 2004]. Assuming still an isotropic applied stress, and assuming that the granular aggregate undergoes isotropic volumetric strains of less than ~20%, the resulting model for compaction of a face centered cubic (FCC) packing of grains by diffusion-controlled creep can be written in the form

$$\dot{\varepsilon}_{diff} \approx \frac{AaZ^* V_{m,s}\sigma_{eff}}{RTd^3 e_v^2} \qquad (3)$$

This applies provided that stresses are low enough (less than 5–10 MPa for ionic solids at room temperature) to allow the standard approximation $\left(e^{\sigma_{eff}V_{m,s}/RT} - 1\right) \approx \sigma_{eff}V_{m,s}/RT$ for the excess solubility developed at grain contacts relative to pore walls [de Meer and Spiers, 1997; Lehner, 1995; Spiers and Schutjens, 1990; Spiers et al., 2004]. Here $\dot{\varepsilon}$ represents the volumetric strain rate defined as $\dot{\varepsilon} = -\dfrac{\dot{V}}{V} = -\dfrac{1}{V}\dfrac{dV}{dt}$, σ_{eff} is the applied effective stress defined as $\sigma_{eff} = \sigma_n - P_f$, $e_v = -\Delta V/V_0$ is the engineering volumetric strain, d is the aggregate grain size, T is absolute temperature, R is the gas constant, a is a geometric factor related to grain packing (a is equal to $3/\pi\sqrt{2}$ for an FCC pack), and A is a geometric constant with a value of 144 (for an FCC geometry, see also Spiers and Schutjens [1990]). Note that V is the instantaneous volume of a representative element of the aggregate, while V_0 is its initial volume. Engineering strain e_v is used instead of natural strain ε for easy comparison with experiments, since in experiments e_v is directly measured in terms of displacement or sample volume change. Z^* is the effective grain boundary diffusivity product defined as

$$Z^* = D_{gb}CS \qquad (4)$$

where D_{gb} is the diffusivity, C the solubility of the solid in the grain boundary solution phase (measured in volume fraction, i.e., volume of solid per volume of solution), and S is the average grain boundary fluid thickness. In the case of an island-and-channel model $S = \delta(1 - \alpha)$, where δ is the grain boundary width and α is the volume fraction of the boundary occupied by solid material (islands). For an adsorbed grain boundary film, $S = \delta$, and any effects of adsorbed film thickness on diffusion are accounted for via the term $D_{gb}C$ [Koelemeijer et al., 2012; Watanabe and Peach, 2002].

[8] When interfacial reactions in a solid/liquid system are rate limiting, the rate of compaction can be written as

$$\dot{\varepsilon}_{int} \approx \frac{BaI^* V_{m,s}\sigma_{eff}}{RTde_v^b} \qquad (5)$$

where I^* is the rate coefficient for either the dissolution or precipitation reaction, depending on which one is rate

controlling [see de Meer and Spiers, 1995, 1997; Raj, 1982; Spiers et al., 2004]. Note that $B = 6$ and $b = 1$ for dissolution-controlled creep, while $B = 3$ and $b = 2$ for precipitation-controlled pressure solution creep.

2.2. An Extended Model for Compaction by Pressure Solution Creep

[9] In the following, the above models (equations (3) and (5)) for densification by pressure solution creep under the action of an applied effective stress are extended to take into account the effects of interfacial energy. In deriving these creep models, the following assumptions are made: (1) densification is assumed to occur by intergranular pressure solution; (2) all mechanical work done is dissipated by the pressure solution process and used in modifying grain pore surface areas and hence total interfacial energy; (3) all dissipation is assumed to occur by one of the three serial steps of diffusion, dissolution or precipitation, each operating in a series of steady states under chemically closed system conditions; (4) grain-to-grain contacts remain macroscopically flat during compaction while the free grain surfaces remain spherical; (5) grain-to-grain contacts are assumed to possess a "dynamically stable" island-channel structure [Lehner, 1990; Raj, 1982; Spiers and Schutjens, 1990; van Noort et al., 2008b]; (6) strains are assumed to be small, that is, $e_v < 20\%$, so that grain diameters do not change much during compaction and grain contacts do not overlap. Note that assumptions (4) and (5) are convenient for clarity but are nonessential.

[10] The idealized granular aggregate is now assumed to have a face centered cubic (FCC) packing and is subjected to an applied effective stress, $\sigma_{eff} = \sigma_n - P_f$, which is hydrostatic in nature. Individual grain contacts remain treated as shown in Figure 1. Making use of equations (1) and (2), with $(1/r_1 + 1/r_2) = 4/d$, the difference in the solid-phase chemical potential between grain boundary dissolution and pore wall precipitation sites is now approximately given by

$$\Delta\mu = \mu_{gb} - \mu_p = \left[(\sigma_n - P_f) - \frac{4\gamma}{d}\right]V_{m,s} \qquad (6)$$

assuming the differences Δf^s and $\Delta V_{m,s}$ in the molar free energy and molar volume between the two sites may on average be neglected. The normal stress σ_n in this equation thus represents the mean normal stress at the grain-to-grain contacts. Furthermore, the area of the contact is given as $A_c \approx \pi d^2 e_v/6$, for strains of less than 20% [Spiers and Schutjens, 1990]. The stress concentration at the grain contact is given as the area occupied by the grain, $A_g = a^* d^2$, over the area occupied by the contact A_c. In general, this means that the stress concentration factor is a/e_v, where $a = 6a^*/\pi$ and a^* are geometric factors, depending on grain packing. Now, a consideration of the force balance at grain contacts shows that

$$\sigma_n \approx \frac{a\sigma_{eff}}{e_v} + P_f \qquad (7)$$

thus reducing equation (6) to

$$\Delta\mu \approx \left(\frac{a\sigma_{eff}}{e_v} - \frac{4\gamma}{d}\right)V_{m,s} \qquad (8)$$

Assuming one of the three serial steps of dissolution, diffusion or precipitation is rate limiting, and coupling the rate equations for linear crystal growth/dissolution or Fick's law with the driving force for solution transfer, constitutive equations for densification by pressure solution, including the effects of both interfacial energy γ and effective stress σ_{eff}, can be obtained in the same manner underlying equations (3) and (5). The classical models for pressure dissolution are then modified in that the driving force $\Delta\mu$ is now given by equation (8).

[11] For the diffusion-controlled case the result obtained is,

$$\dot{\varepsilon}_{diff} = \frac{AZ^* V_{m,s}}{RTd^3 e_v} \left(\frac{a\sigma_{eff}}{e_v} - \frac{4\gamma}{d} \right) \tag{9}$$

For the interfacial reaction-controlled case, the result is

$$\dot{\varepsilon}_{\mathrm{int}} = \frac{CI^* V_{m,s}}{RTde_v^c} \left(\frac{a\sigma_{eff}}{e_v} - \frac{4\gamma}{d} \right) \tag{10}$$

where $C = 6$ and $c = 0$ for dissolution control, and where $C = 3$ and $c = 1$ for precipitation control. Note that these new models predict a reduced driving force and reduced rate of compaction by pressure solution as $4\gamma/d$ approaches $a\sigma_{\mathrm{eff}}/e_{\mathrm{v}}$, that is, in fine-grained material subjected to low effective stresses and relatively large strains. Moreover, the models predict a minimum stress, that is, a yield stress, required for pressure solution to occur, given as $\sigma_{\mathrm{eff}} = 4\gamma e_{\mathrm{v}}/ad$. This corresponds to zero driving force for pressure solution creep at the condition $\dot{\varepsilon} = 0$, which represents the situation where the surface free energy-related term in equations (9) and (10) balances the stress-related term. As this zero driving force condition is approached with increasing strain (e_{v}) at constant applied stress, or with decreasing applied stress, an island-channel contact structure will undoubtedly evolve, due to the onset of internal contact healing effects in such a way that both Z^* and I^* decrease. At sufficiently low applied stress, large contact area, small grain size and in systems with large γ values, $4\gamma/d$ will exceed $a\sigma_{\mathrm{eff}}/e_{\mathrm{v}}$ and contact healing and neck growth will be favored over pressure solution, as matter is transported from pore walls to grain contacts.

3. Pressure Solution Creep Experiments on NaNO$_3$ as an Analog System

[12] The present experiments consist of uniaxial (1-D) compaction experiments performed on granular NaNO$_3$ under both dry and wet conditions, that is, with laboratory air or saturated NaNO$_3$ solution filling the pores. The experiments were performed at room temperature under drained conditions, maintaining the pore fluid pressure at atmospheric levels. The aim was to test the applicability of the above models to a high-solubility material (10.8 mol/l at 20°C) expected to exhibit solution transfer phenomena under easily accessible conditions.

3.1. Starting Material

[13] The tests were performed on 14 different grain size fractions of fine-grained NaNO$_3$, having mean grain sizes of $8 \pm 2~\mu$m, $11.5 \pm 2~\mu$m, $15 \pm 3~\mu$m, $20 \pm 3~\mu$m, $22 \pm 3~\mu$m, $27 \pm 7~\mu$m, $39 \pm 5~\mu$m (subspherical), $39 \pm 7~\mu$m (angular), $63 \pm 8~\mu$m, $71 \pm 7~\mu$m, $90 \pm 8~\mu$m, $104 \pm 9~\mu$m, $163 \pm$ 15 μm, and $250 \pm 19~\mu$m. The fractions with a mean grain size of $\geq 39 \pm 7~\mu$m were obtained from as-received, analytical grade NaNO$_3$ (Merck Chemicals) by sieving. Fractions of $39 \pm 5~\mu$m and smaller were prepared by first crushing the unsieved analytical reagent in a ball mill, followed by separation using conventional gravitational settling in NaNO$_3$-saturated, analytical-grade methanol (Baker 99.5% pure). After filtering, the powder was washed with ultrapure hexane (less than 0.05% water) to remove any remaining methanol. The powder was subsequently dried in an oven at temperatures of ~60°C, and stored in a dry room before use. The true average grain size of the final fractions was determined from measurements on SEM micrographs of representative samples. The grain shapes characterizing the individual fractions were more or less equi-axed, with the gravimetrically settled material ($d \leq 39 \pm 5~\mu$m) being subspherical, while the sieved grain size fractions showed angular grain shapes ($d \geq 39 \pm 7~\mu$m).

3.2. Experimental Setup and Procedure

[14] The various grain size fractions were tested at room temperature under dry and wet conditions, using a small-scale, dead-weight, capillary tube setup [see also de Meer and Spiers, 1997; Zhang et al., 2002, 2010; Zhang and Spiers, 2005] (Figure 2). In this setup, a "gap sensor" transducer (Baumer Electric, type IWA 18U 9001) was used to measure displacement (linearity of 0.5%, full scale of 1.5 mm, output signal of 2–8 V). The displacement output signal was logged using a 16-bit A/D converter plus PC, with a logging cycle of 5 s. This enabled displacement versus time data to be recorded with displacement errors of <0.01 μm between adjacent readings, and time errors of <0.001 s. The setup was calibrated for thermal expansion effects related to diurnal temperature cycles. However, the magnitude of these effects was very small and corrections for temperature variations proved unnecessary.

[15] For each experiment, 10.0 ± 0.05 mg of sample material of the selected grain size fraction was deposited into the glass capillary tube setup (internal diameter 2.1 ± 0.05 mm; see Figure 2), with the lower steel piston (~2.00 mm diameter) and supporting brass base in place. The upper piston was then inserted and the sample was loaded with a dead weight of 1500 g, equivalent to an applied axial stress of 0.49 MPa. Samples were allowed to compact dry for 2 h, to achieve a locked aggregate with a well-controlled "starting porosity" (φ_0). Note that porosity was calculated using the sample dimensions and samples mass, assuming a density for NaNO$_3$ of 2.26 g/cm^3.

[16] After dry compaction, the applied dead weight was adjusted to give the desired stress (0.002 to 4.9 MPa) for further testing. The samples were then rapidly flooded with NaNO$_3$-saturated solution by adding solution to the plastic ring reservoir located at the top of the capillary tube (Figure 2), while simultaneously applying a partial vacuum via the evacuation tube in the brass base. When the whole sample was flooded, the evacuation tube was closed, the remaining liquid in the plastic ring reservoir was removed and a drop of silicone oil was added to the reservoir to prevent evaporation, resulting in a closed system. Displacement of the dead weight was then measured as a function of time, using the gap sensor. Experiments were terminated by removing the dead weight, flush drying the sample by
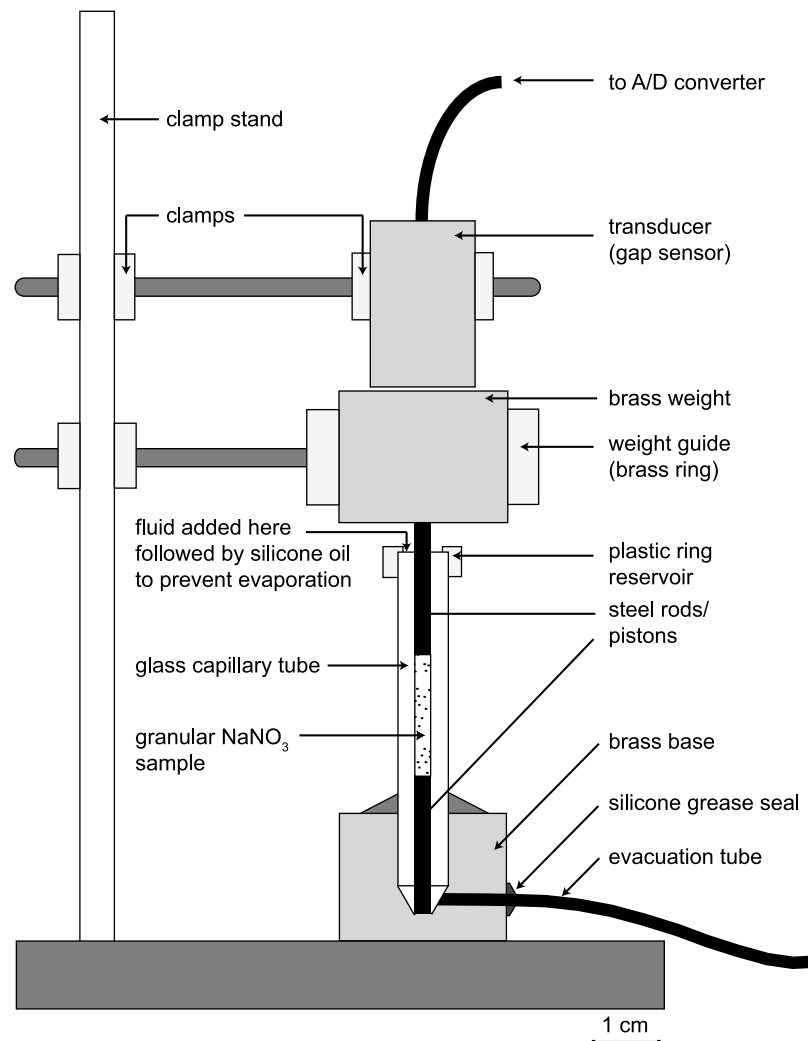
Figure 2. Schematic diagram illustrating the uniaxial glass capillary tube setup used to perform compaction experiments on $NaNO_3$ aggregates in this study.

passing compressed air through the capillary tube, and then carefully pushing the sample out of the tube to be dry-stored prior to thin sectioning and preparation for SEM study.

[17] Control experiments were performed under dry conditions (i.e., without adding $NaNO_3$ solution after initial compaction) and initially dry loading for 2 h, followed by the addition of silicone oil. In addition, we performed wet compaction experiments for various amounts of time (<24 h to up to 2 months), to study microstructural development as a function of compaction time. Experiments using wider capillary tubes (internal diameter 5.0 ± 0.05 mm), employing 55 ± 5 mg samples, allowed for experimentation at low applied stresses (down to 0.002 MPa) using the standard dead weight configuration.

[18] In total, more than 150 experiments were performed, of which around 120 involved wet compaction using saturated solution. The solution was always saturated with the grain size fraction employed in the experiment. As the wet compaction behavior proved to be very sensitive to starting sample porosity (i.e., porosity after dry compaction), narrow ranges of starting porosity were chosen for investigating the

effects of other variables, such as stress or grain size. The 2 mm tubes produced starting porosities in the range 39 to 47%, while the 5 mm tubes in general produced higher initial porosities ($48.5–50 \pm 2\%$). Therefore, the data from the 2 mm and 5 mm tube experiments are treated separately. For the 2 mm tube experiments, initial porosity ranges (φ_0) chosen for assessing the effects of other variables were $40.5 \pm 2.5\%$, $42.0 \pm 2.5\%$ and $45.5 \pm 2.0\%$. Samples with starting porosities outside these ranges were rejected. To avoid duplication of the graphically presented data, and given the very large number of experiments performed, we omitted a table summarizing all the experiments and conditions.

3.3. Friction Determinations

[19] Since one of the aims of the wet compaction tests was to investigate competition between stress-related and interfacial energy-related driving forces for solution transfer, it was necessary to achieve very low stresses, that is, contact stresses of magnitudes comparable with the quantity $4\gamma/d$ (equations (9) and (10)). These low stresses required the
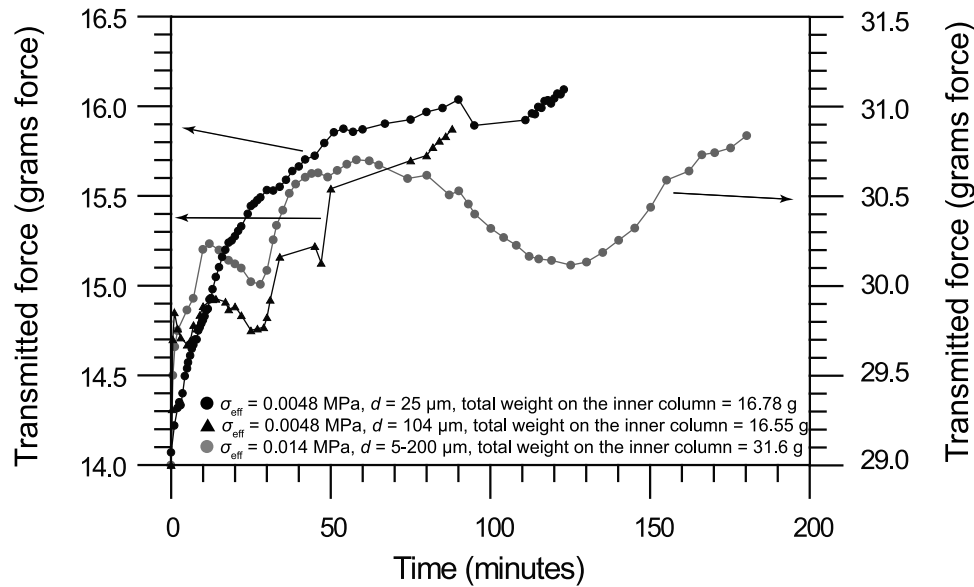
Figure 3. Transmitted force versus time curves, as obtained during friction determinations, illustrating the reduction in force transmitted through the sample column due to friction and adhesion with time. Data for grain sizes fractions of 25 μm, 104 μm, and 5–200 μm. Tube sizes of 5 mm were used. Saturated solution was added at $t = 0$ after dry precompaction.

application of dead weights down to 5 g. Such applied loads are so low that frictional effects at the piston/tube and sample/tube surfaces, or even capillary forces at the fluid menisci, could potentially introduce significant errors in the applied load. Therefore, a number of so-called "friction determinations" were performed to quantify these effects.

[20] Sample preparation for the friction experiments was the same as for compaction experiments. After 2 h of dry compaction, the glass tube, including pistons and sample, was removed from the brass base and placed in a clamp stand positioned over a balance. The tube was clamped in such a way that the force transmitted through the inner column (consisting of the lower piston, sample and upper piston) was measured by the balance, while the weight of the glass capillary tube (outer "clamped" column) was not. In this way, frictional forces between the inner column and the glass tube inner wall, and adhesion forces due to the fluid-air menisci at the pistons, could be measured as a reduction in applied dead weight observed on the balance.

[21] After setting up the dry sample and applying an appropriate dead weight, saturated solution was added to the reservoir on top of the capillary tube. The fluid then rapidly spread through the porous sample due to capillary action. Only a small excess of fluid was added. The fluid did not run out of the capillary tube at the lower piston, because of capillary forces.

[22] The friction determinations were performed using the smallest weights employed in the regular compaction experiments, that is, 11 g and 25 g for the 2 mm tube, and 5 g and 25 g for the 5 mm tube. The influence of grain size was investigated as well, using grain size batches of 25 μm, 104 μm and 5–200 μm fractions. After fluid infiltration, the force transmitted to the microbalance was recorded with time, taking measurements every 20 s at the start of

each experiment, decreasing to every 10 min by the end of the experiment. The largest deviation in measured force from the imposed force (weight) occurred while the sample was still dry, when fluid passed through the sample, and shortly after this, as illustrated in Figure 3. Addition of the fluid at time $t = 0$ was followed by a sharp increase in the transmitted force measured with time. Every curve showed a rough wavelike pattern after or even during the initial sharp increase. This wavelike pattern is typical of frictional force versus time experiments in such configurations [*Ravikiran*, 1995]. The maximum deviation in transmitted from applied force was observed at the start of the experiments, when the applied stress was reduced by as much as 17% for the very low stress experiments (≤0.005 MPa). Because the absolute weight reduction did not vary much with applied weight, the relative error decreased rapidly with increasing applied stress (e.g., 8% for 0.014 MPa and 4% for 0.025 MPa). With increasing time, the remaining error due to friction and adhesion was ~1–4%. Because relatively high-stress experiments (>1 MPa) can achieve several percent of strain at the start of the experiment, a window of minimum strain and time can be used to restrict errors due to friction and adhesion. On this basis, it was decided to reject data obtained below 10% strain, unless obtained after more than one hour of elapsed time.

3.4. Data Processing

[23] Instantaneous volumetric strain was calculated directly from the displacement versus time records obtained for each experiment in terms of the engineering strain, defined as $e_v = -\dfrac{\Delta V}{V_0}$, which for our uniaxial compaction experiments is equal to $e_v = -\dfrac{\Delta L}{L_0}$. Instantaneous strain
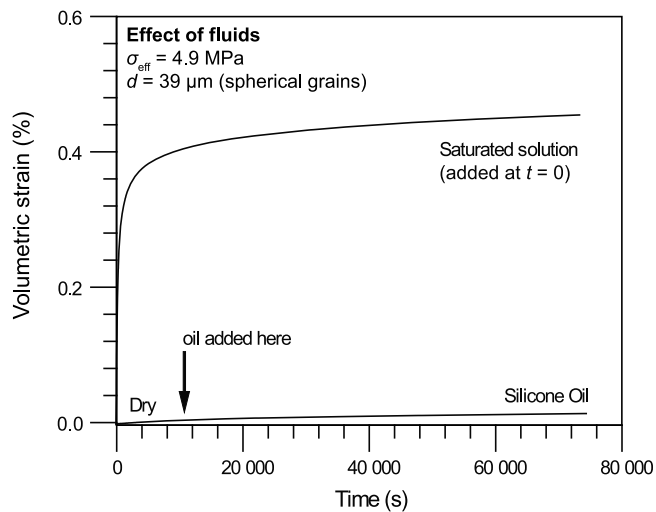
Figure 4. Comparison of creep behavior of granular $NaNO_3$ loaded initially dry followed by saturation with oil, versus a sample loaded dry then saturated with $NaNO_3$ solution at $t = 0$ after dry compaction beforehand. Applied stress was 4.9 MPa and the average grain size was 39 μm (spherical grains) for both experiments.

rates were calculated using the three-point central difference method, using the definition $\dot{\varepsilon} = -\dfrac{1}{L}\dfrac{dL}{dt}$. For the first and last data points of each test, and for data points where the time interval to the next data point was larger than 7200 s, the strain rate was interpolated using two data points only. Taking into account all sources of error in measuring displacement and time, the maximum error in calculating strain rate is estimated to be typically around 4%, reaching 10% at strain rates $<10^{-7}$ s^{-1}.

3.5. Microstructural Methods

[24] Scanning electron microscopy (SEM) and transmission optical microscopy were used to study the starting material, the dry-compacted and the wet-compacted samples. Prior to preparation, the compacted samples were cut in half. One half was used for SEM, the other half for thin section preparation. For SEM work on the starting powder, the material was distributed on SEM sample stubs coated with a dry layer of colloidal carbon adhesive and subsequently gold-coated. After drying, the compacted samples were mounted with colloidal carbon adhesive to SEM stubs and both carbon- and gold-coated. For optical microscopy, thin sections of the compacted samples were prepared by impregnating them with epoxy resin containing a blue dye and then polished, using Bruers SiC-4000 paper, to a thickness of $\sim$8–50 micron (depending on the grain size). Final polishing was done in a low humidity room. For optical microscopy, a coverslip was then glued onto the sample, with epoxy resin, to prevent moisture corrupting the microstructure after preparation. Some thin sections were used for uncovered SEM study. After polishing, most of these were etched with Zn-saturated glacial acetic acid for 10–30 s and then rinsed with ultrapure hexane (<0.05% water). Since zinc is preferentially adsorbed onto the resin surface, clear contact between grains and epoxy-filled pores

was obtained using this method, especially highlighting grain/pore interfaces.

4. Results

4.1. Mechanical Data

[25] During initial dry compaction at 4.9 MPa, all samples showed an instantaneous shortening of 0.04–1% followed by minor creep. Samples that were subsequently loaded at lower effective stress, either dry or with added oil, showed little or no additional creep.

[26] In contrast to dry or oil-saturated samples, wet samples showed very rapid compaction creep (Figures 4 and 5). Figure 5a shows typical wet creep curves, obtained at different stresses for material with a fixed starting grain size ($d = 39$ μm; spherical). Note the large range of stresses used (three orders of magnitude; see Figure 5a). The experiments performed at higher stresses clearly tended to produce more
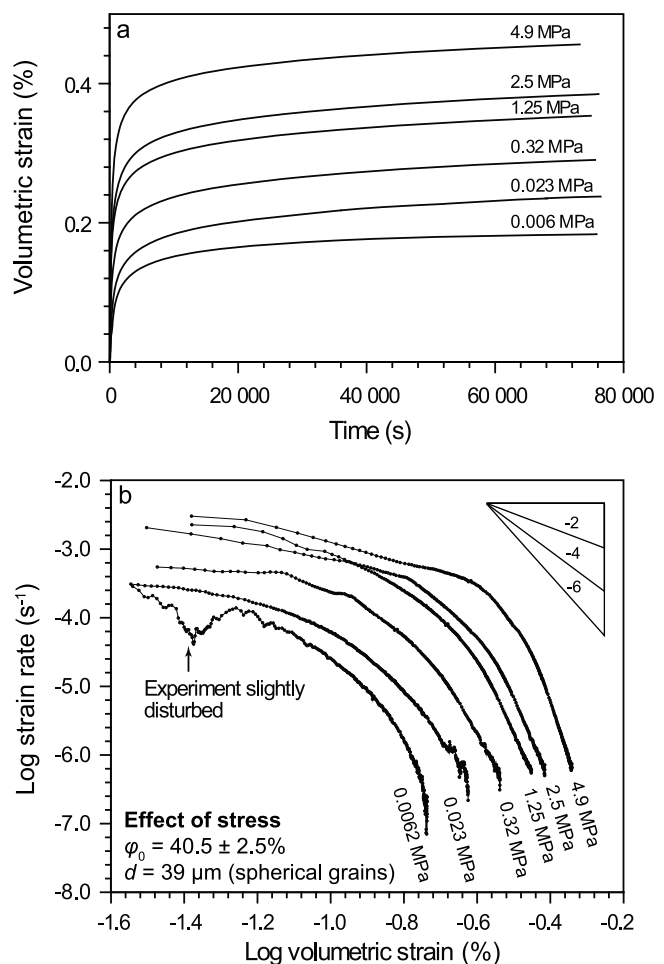

Figure 5. Compaction creep data for the wet $NaNO_3$ experiments performed for the effective stress indicated at each curve ($\varphi_0 = 40.5 \pm 2.5\%$; $d = 39$ μm – spherical grains). (a) Volumetric strain ev versus time plot; (b) log volumetric strain rate versus log volumetric strain plot derived from Figure 5a, showing how the compaction rate ($\dot{\varepsilon}$) at fixed creep strain (ev) increases with increasing effective stress. Inset triangles show slopes for comparison with the data.
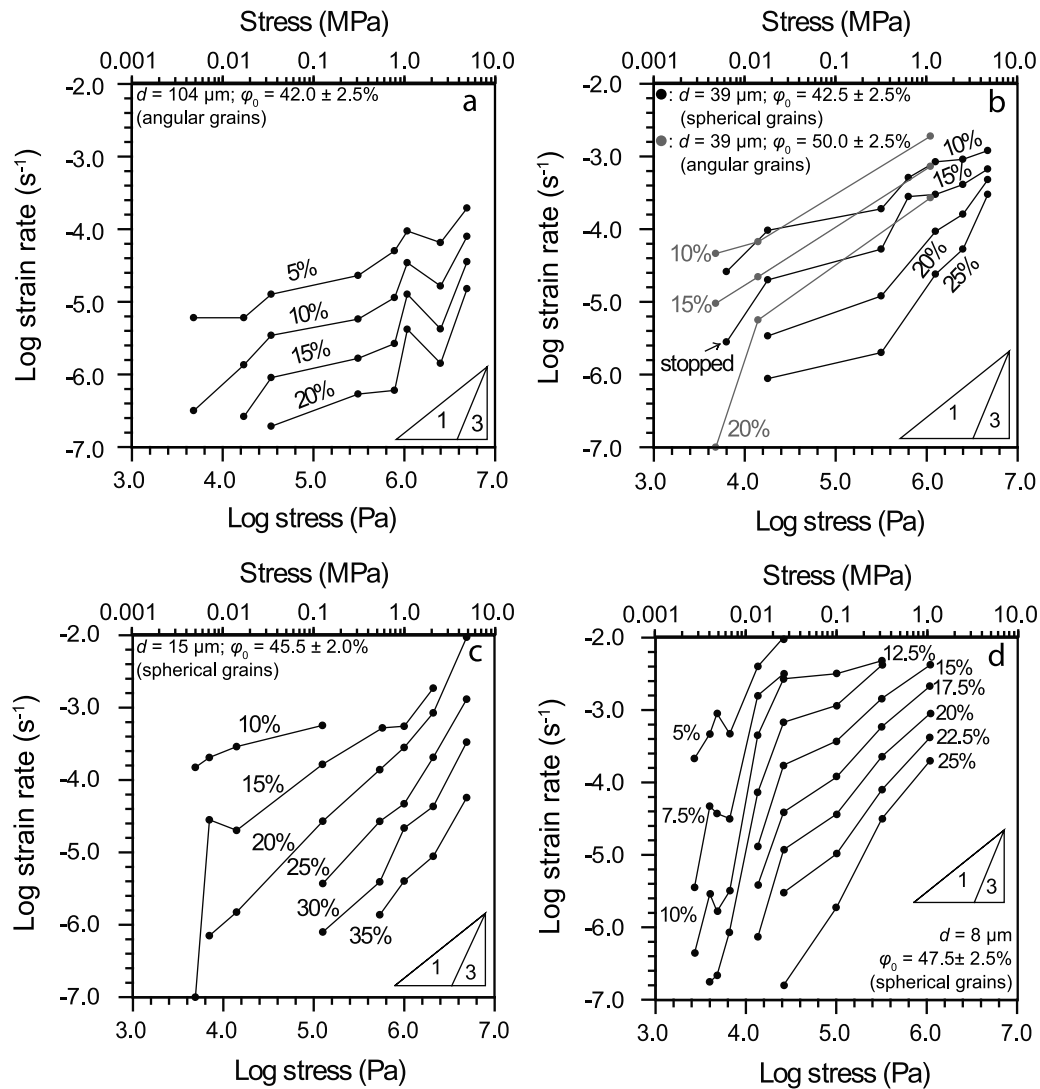
Figure 6. Compaction creep data for the wet $NaNO_3$ experiments, showing the effect of effective stress on strain rate: (a) $d = 104$ μm (angular grains), $\varphi_0 = 42.0 \pm 2.5\%$; (b) $d = 39$ μm (spherical grains), $\varphi_0 = 42.5 \pm 2.5\%$, and $d = 39$ μm (angular grains), $\varphi_0 = 50.0 \pm 2.5\%$; (c) $d = 15$ μm (spherical grains), $\varphi_0 = 45.5 \pm 2.0\%$; (d) $d = 8$ μm (spherical grains), $\varphi_0 = 47.5 \pm 2.5\%$. Inset triangles show slopes for comparison with the trends in the data. Note that the percentages next to the curves denote the volumetric strain at which the data point was taken.

or faster creep, reaching nearly full densification ($\sim$40% strain) in 24 h. From the corresponding log strain rate versus log volumetric strain plot (Figure 5b), it can be seen that volumetric strain rates decrease with increasing strain. The individual data sets can be described by a power law function of the form $\dot{\varepsilon} \propto e_v^k$, with the data showing slopes (k exponents) ranging from -2 to -5 at strains around 10–20%. Toward higher strains, the strain rates decrease very rapidly with increasing strain, indicating that compaction slows down and reaches immeasurable rates or even comes to a halt. For the highest applied stress ($\sigma_{eff} = 4.9$ MPa), a steep decrease in strain rate can be observed from $\sim$20% strain to nearly full densification ($\sim$2% porosity left). At lower stresses, a similar shape is observed but with creep slowing down sharply at lower volumetric strains. For

example, the experiment at 0.0062 MPa attained 18.3% strain before it stopped, which is long before full densification of the material.

[27] Plots of compaction rate ($\dot{\varepsilon}$) versus applied effective stress (σ_{eff}) and grain size (d), constructed from our creep curves and corresponding strain rate versus volumetric strain data (cf. Figure 5), are shown in Figures 6 and 7. Figure 6 shows log strain rate versus log stress plots derived from experimental data similar to those plotted in Figure 5b, at constant strains and for various grain sizes. The slopes of the curves plotted in Figure 6 represent the stress exponent (n) in an empirical power law description of the form $\dot{\varepsilon} \propto \sigma^n$, applied for fixed strain (or porosity). At stresses in the range 0.022–4.9 MPa, the stress exponent is close to 1 on average. For coarser grain sizes (104 μm; Figure 6a) the stress
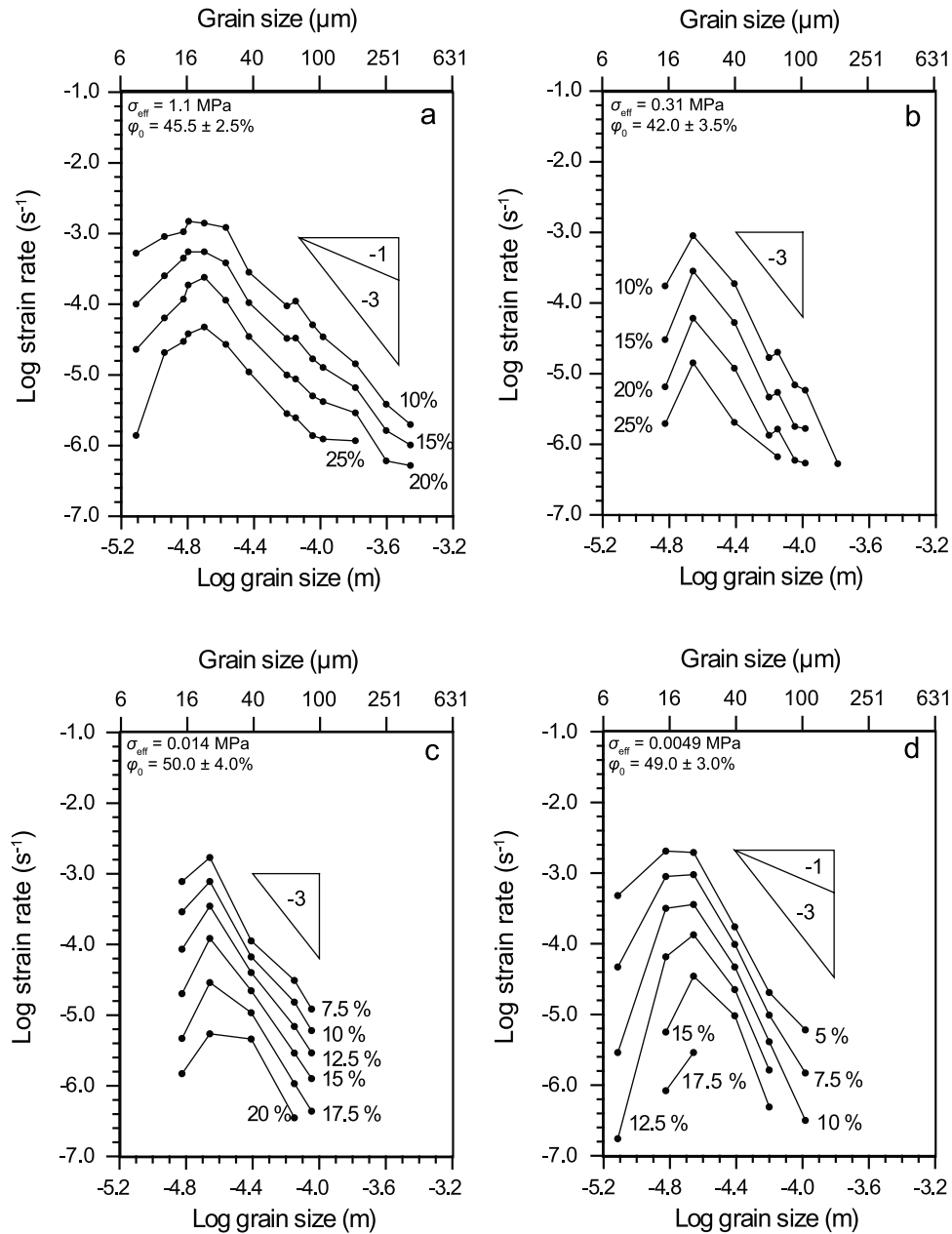
Figure 7. Compaction creep data for the wet $NaNO_3$ experiments, showing the effect of grain size on strain rate: (a) σ_{eff} = 1.1 MPa, φ_0 = 45.5 ± 2.5%; (b) σ_{eff} = 0.31 MPa, φ_0 = 42.0 ± 3.5%; (c) σ_{eff} = 0.014 MPa, φ_0 = 50.0 ± 4.0%; (d) σ_{eff} = 0.0049 MPa, φ_0 = 49.0 ± 3.0%. Inset triangles show slopes for comparison with data trends. Note that the percentages next to the curves denote the volumetric strain at which the data point was taken.

exponent is a little less than 1 ($n \approx 0.7$), while for finer grain sizes (8 μm; Figure 6d), n is somewhat more than 1 ($n \approx 1.3$ for stresses down to 0.022 MPa) increasing to ~2 at the higher strains achieved. Toward the lowest stresses (0.022 MPa), strain rates suddenly decrease for grains with $d \leq 39$ μm, producing a sharp increase in slope n (see Figures 6b–6d). While, this effect is only seen for a single data point for the grain size fractions of 39 μm and 15 μm (Figures 6b and 6c), the effect is clearly established for the finest grain size fraction of 8 μm, as seen in Figure 6d.

[28] The grain size dependence of strain rate is shown in the form of log strain rate versus log grain size plots in Figure 7, for the constant applied effective stresses and strains shown. Individual data sets can be described by a power law of the form $\dot{\varepsilon} \propto d^m$. At relatively coarse grain sizes (>20 μm), an m value, that is, slope, of about −3 is observed. However, toward finer grain sizes (<20 μm), an abrupt switch to a positive dependence of densification rate on grain size is observed, as strain rate decreases with decreasing grain size, displaying a grain size exponent

(slope) of $m = +1$ to $+6$, increasing with increasing amount of total volumetric strain (Figure 7a).

4.2. Microstructural Observations

4.2.1. Starting Powders

[29] SEM micrographs of the starting fractions were used to determine the true average grain sizes (section 3.1). The starting powders consisted of granular aggregates of mostly discrete equi-axed particles with reasonably uniform size. The fractions obtained by gravitational settling in methanol ($d \leq 39$ μm) showed subspherical grains, whereas the equivalent sieved fractions showed angular grain shapes. Rounding may have occurred by minor dissolution in the methanol settling fluid, although this was presaturated with respect to NaNO$_3$. Some of the grains in the fractions obtained by sieving (≥ 39 μm) could be recognized as cleavage rhombohedra, but otherwise no distinct preferential shapes or orientations were observed. In the gravity-settled material minor interparticle "welding," neck growth and sintering features were present. Rare pressure solution-like microstructures (indentations) were also found. The amount of crystal plastic deformation present in the starting material was investigated by means of optical microscopy performed on powdered material immersed in a droplet of paraffin between two glass plates. Only a few grains showed undulatory optical extinction evidencing plastic deformation. However, $e\{01\bar{1}2\}$ deformation twins were found in some larger grains. The total proportion of twinned grains was estimated to be $\sim$3% by point counting.

4.2.2. Dry Compacted Samples

[30] SEM and thin section studies were carried out on dry compacted samples to assess the extent of deformation by any additional mechanisms besides intergranular sliding and rearrangement. The typical granular/porous microstructure observed is shown in Figure 8a. No undulatory extinction was observed using cross polarized light. Evidence for grain fracturing or contact crushing was found in only a few grains within each sample. With respect to mechanical twinning, no visual difference could be observed between the proportion of twinned grains in the dry compacted sample and the starting material. As in the (sieved) starting fractions, only occasional grains showed microstructural features, such as indented grains, similar to those characteristic of pressure solution creep.

4.2.3. Wet Compacted Samples

[31] We observed three main microstructural regimes in the wet-compacted samples, depending on effective stress, grain size, and total volumetric strain achieved (Figures 8b–8f).

[32] 1. *Highly stressed, finer-grained* samples ($\sigma_{eff} > 0.3$ MPa, $d \leq 39$ μm), attained high volumetric strains (i.e., $e_v > 20\%$) within 24 h of flooding with saturated solution and accordingly show low final porosities. At the highest stresses of more than 1 MPa, only 8–12% porosity remains after this period of compaction, for grain sizes in the range 20 to 39 μm. These samples exhibit a dense polygonal microstructure of well-fitting grains, often with well-developed triple junctions
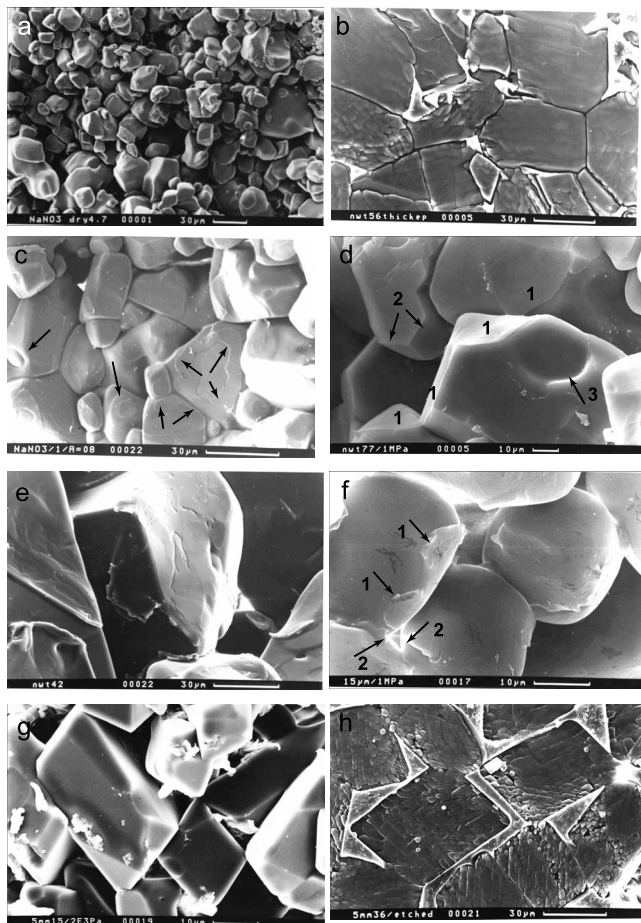

Figure 8. SEM images of compacted NaNO$_3$ aggregates. (a) Dry NaNO$_3$ compacted at an effective stress of 4.9 MPa and with an initial grain size of 15 μm. (b) Finer-grained, wet NaNO$_3$ ($d = 39$ μm, angular grains) compacted at 1 MPa effective stress for 24 h, up to 36% volumetric strain displaying a dense structure of polygonal grains and clear triple junctions. The white areas represent resin-filled porosity, which shows bright contrast due to Zn-absorption by the epoxy resin after Zn-acetate treatment. (c) Finer-grained NaNO$_3$ ($d = 15$ μm, angular grains) compacted wet at an effective stress of 1 MPa. Note that the former grain-to-grain contacts show closed ring-shaped internal structures (see arrows). (d) Wet-compacted, finer-grained NaNO$_3$ ($d = 39$ μm, angular grains), deformed at 1 MPa effective stress. Note the former contact surfaces (1), the overgrowth in the pore region (2) and a "pit" that most likely results from dissolution (3). (e) Coarser-grained, wet NaNO$_3$ ($d = 104$ μm) compacted for 24 h at 1 MPa showing a rough contact surface, indicative of pressure solution features. (f) Finer-grained NaNO$_3$ ($d = 15$ μm, subspherical grains) compacted wet for 15 min at 1 MPa, resulting in 18% volumetric strain. Note that the grain size is still subspherical and that the former grain-to-grain contacts show open ring contacts (1) and possibly neck growth (2). (g) Very fine grained NaNO$_3$ ($d = 8$ μm) compacted wet at an effective stress of 0.002 MPa, reaching a volumetric strain of 3% after 48 h of compaction. Note that the grain shape has changed from subspherical to euhedral, displaying clear grain facets suggestive of dissolution-precipitation processes. (h) Finer-grained, wet NaNO$_3$ ($d = 39$ μm, angular grains) compacted at 0.0048 MPa for ~24 h, reaching 21% volumetric strain. White-rimmed epoxy-filled pores show high contrast due to Zn-acetate treatment.

(Figure 8b). For the finest initial grain sizes of less than 20 μm, less strain was achieved under otherwise identical conditions, and though still quite dense the microstructures show higher residual porosity (Figure 8c). These particular samples also show increased final grain sizes, indicating grain growth during compaction, as well as the development of closed, concentric ring structures formed within grain-to-grain contacts (Figure 8c).

[33] 2. In the *high-stress* experiments on *coarser-grained* samples ($\sigma_{\text{eff}} = 0.3$ MPa for $d \geq 63$ μm, and $\sigma_{\text{eff}} \geq 1$ MPa for $d \geq 104$ μm), lower final strains (<20%) were obtained after 24 h of compaction. Similarly low strains were obtained for finer grain sizes compacted at high stresses for shorter compaction times. The microstructures of these high-stress and low-to-intermediate strain samples show typical pressure solution features such as grain-to-grain indentations, dissolved contacts and overgrowths in the pores (see arrow 2 in Figure 8d, fine grain size), as well as rough grain contacts (Figure 8e, coarse grain size). Figure 8f shows that in finer-grained material, briefly compacted to low compaction strains, porosity remained high and the grain shape remained subspherical. Open, concentric ring structures and neck growth features are also developed within and at the margin of grain contacts in such samples (see arrow 1 in Figure 8f). In the highest stress (4.9 MPa) experiments showing relatively high final porosity, large dissolution pits developed at grain contacts. These were absent at lower stresses and in samples compacted to higher densities.

[34] 3. The *low-stress experiments* ($\sigma_{\text{eff}} < 0.01$ MPa) show distinctly different microstructures especially in the finest-grained samples. In these samples ($d \leq 39$ μm), (sub)euhedral grains developed within 24–48 h, both from subspherical starting fractions (Figure 8g) as well as from the angular 39 μm grain size fraction (Figure 8h). For the latter fraction, only shape change occurred, while for the subspherical grains of $d < 39$ μm grain growth occurred simultaneously. The 8 μm spherical grain size fraction grew to approximately 12 μm and the 15 μm grain size fraction to an average of 24.8 μm within 24 h. For larger grain sizes ($d > 39$ μm) and shorter compaction times, less extensive grain shape changes were observed. Pressure solution-type features, such as contact dissolution and indentation were observed (similar to those shown in Figures 8d and 8f). Also, in samples subjected to longer compaction times, distinctive rim structures were observed on former grain contacts (similar to those shown in Figure 8c).

[35] In general, three different grain boundary structures can be observed in the wet compaction experiments: (1) grain boundaries or contact areas showing a rough structure, characterized by indentation and contact dissolution features (Figure 8e); (2) closed rim structures indicated by ring-like or neck-like precipitation features within and at the margin of grain-to-grain contacts (Figure 8c); and (3) open rim structures that are similar in appearance to the closed rim structures with the exception that they are open on at least one side (Figure 8f).

[36] Rough grain boundary structures, as described under point 1, are observed in high-stress samples at low/intermediate strains (final porosity >10%; see Figure 8e). However, occasional rough contacts have also been observed in very low stress, coarser grain size experiments. In such cases, the rough structures are associated with small,

indenting contact areas, suggesting an association with relatively high contact stress.

[37] Closed rim structures (point 2) were observed in the high-stress/high-strain regime and also in the low-stress regime. In both cases, long compaction times were involved (24–48 h), though the amount of strain obtained was very different for each regime.

[38] Contact rims and rings that are open on at least one side (point 3) are observed together with rough contact structures, as well as with closed rim structures, and seem to represent an intermediate or incomplete stage of forming closed rim/ring structures.

5. Discussion

[39] The uniaxial compaction experiments have demonstrated that dry, fine-grained $NaNO_3$ aggregates with a constant starting porosity show little or no densification creep when loaded dry at stresses up to 4.9 MPa. This rules out significant time-dependent deformation by plasticity or intergranular sliding under these conditions. Furthermore, addition of silicone oil to the dry, loaded samples has little effect, eliminating any purely mechanical effect of adding a fluid. However, in the presence of saturated $NaNO_3$ solution, rapid compaction creep is observed, suggesting a fluid-enhanced deformation process. The presence of indentations, truncations, dissolution pits and other grain contact roughness structures indicates that an important role was played by grain boundary diffusional pressure solution creep. In the remainder of our discussion, we compare our experimental results with our pressure solution models represented in equations (9) and (10), identifying which is most consistent with our data.

[40] On the basis of both mechanical and microstructural observations, two different behavioral regimes can be discerned, namely a low-stress regime (<0.025 MPa) and a high-stress regime (>0.025 MPa). The high-stress regime can be further divided into low-strain ($e_v = 10$–20%) and high-strain ($e_v > 20\%$) fields. With respect to grain size, a further subdivision in behavior can be recognized. To avoid too many subdivisions, the effects of grain size will be discussed in more detail under the high- and low-stress regimes described below. Recall that mechanical data obtained at strains lower than 10% are not considered due to the influence of frictional/adhesive forces generated by load transmitted to the sample.

5.1. The High-Stress Regime: Low- and High-Strain Fields

[41] At *low volumetric strains* ($e_v = 10$–20%), the wet compacted samples tested at $\sigma_{\text{eff}} > 0.025$ MPa showed strain rates ($\dot{\varepsilon}$) approximately proportional to $\sigma_{\text{eff}}^{0.7 \text{ to } 1.3}$, $1/d^3$, and to $1/e_v^{2 \text{ to } 4}$, for $d > 20$ μm (Figures 6 and 7). Based on the grain-size dependence, this behavior is not consistent with reaction controlled pressure solution creep (equation (10)). However, it is broadly consistent with diffusion control (equation (9)), for the case that the interfacial energy-related term ($4\gamma/d$) is negligible in comparison with the stress-related driving force term ($a\sigma_{\text{eff}}/e_v$). Evaluation of these two terms using the values $\sigma_e > 0.025$ MPa, $0.1 \leq e_v \leq 0.2$ and $d > 20$ μm, putting $\gamma \approx 0.27$ J/m^2 for $NaNO_3$ [*Dzerhakhov et al.*, 1986], and taking $a = 3/(\pi\sqrt{2})$, assuming face

centered cubic packing, shows that for the stress range investigated ($\sigma_{\text{eff}} > 0.025$ MPa) it is indeed expected that ($a\sigma_{\text{eff}}/e_v) \gg (4\gamma/d$). In addition, the observed mechanical behavior is associated with indentation/truncation microstructures (Figure 8d), as well as with rough grain boundary structures (Figure 8e), suggesting that pressure solution creep is the dominant deformation mechanism with an island/channel grain boundary structure present within the contacts.

[42] For grain sizes $d < 20$ μm, a marked decrease in strain rate with decreasing grain size was observed (see Figures 7a and 7b) and less strain was obtained compared to coarser-grained samples under otherwise similar conditions. Microstructural observations indicated little or no grain growth (Figure 8f), so that the final grain size cannot explain the decrease in strain rate. Grain contacts often show open internal or marginal ring-shaped structures, suggesting that (partial) neck growth took place in the finer-grained samples, even at high-stress conditions (e.g., Figure 8f). This behavior is consistent with the predictions of equation (9) (and also of equation (10)) when the $4\gamma/d$ term is less than $a\sigma_{\text{eff}}/e_v$ but approaching it in magnitude, so that the driving force for pressure solution decreases (with decreasing d). Inserting the above values into these two terms shows that this is indeed the case when d falls to approximately 10 μm.

[43] At *high volumetric strains* ($e_v > 20\%$), the observed wet compaction behavior for grain sizes >20 μm still showed a grain size dependence with an exponent close to -3 (Figure 7), again pointing to diffusion and not reaction controlled pressure solution. However, the sensitivity of strain rate to stress increased relative to that seen at low strains, and the sensitivity to e_v deviated strongly from the model of equation (9) (see Figures 5 and 6). Specifically, with increasing e_v the exponent to volumetric strain increases rapidly from 2 to more than 5 ($\dot{\varepsilon} \propto 1/e_v^{2-5}$), and near the end of some experiments approaches infinity as the strain rate approaches zero (Figure 5). The rapid decrease in strain rate coincides with the occurrence of closed, ring-type grain contact structures (Figure 8c), in contrast to the rough contacts observed at low volumetric strain (Figure 8f). This suggests that peripheral neck growth processes driven by interfacial energy forces become significant at these high strains, as a result of increased contact area and lower contact stress. Many of the high-stress (>1 MPa) experiments effectively stopped creeping as the porosity approached 10–12%, while experiments at lower stresses stopped at higher porosities (i.e., at lower strains; Figures 5 and 6). This is consistent with the notion that densification decelerates and eventually stops ($\dot{\varepsilon} \rightarrow 0$) when the driving force due to the applied stress (i.e., the term $a\sigma_{\text{eff}}/e_v$) approaches the driving force due to surface forces ($4\gamma/d$); see equations (9) and (10). In that case, contact healing will occur as the chemical potential of dissolved solid in the pores approach the mean solid potential within the grain boundary. An alternative explanation for the cessation of creep at large strains might be that as grain contact stresses become sufficiently low, peripheral neck- or island-growth processes dominate over pressure solution creep.

[44] Closed-rim grain contact features (e.g., Figure 8c) were most frequently observed at high volumetric strain ($e_v > 25\%$). Moreover, combinations of both (partly) developed rim or neck structures plus an internal rough grain boundary surface were observed at ~20% volumetric strain (Figure 8e), indicating a transition from nonequilibrium pressure solution creep at lower strains to a neck-growth or internal island-growth type of process at higher strains. However, it is also possible that rapid densification at the start of the experiments deposited material just outside the grain boundary, which subsequently became accreted into the contact rim, producing features similarly to those seen in Figure 8f.

[45] For experiments performed on material with a grain size <20 μm, the same decrease in strain rate with decreasing grain size is observed at high strains as in the low-strain field described above. In experiments on samples with these fine grain sizes, performed at an applied stress of more than 1 MPa, volumetric strains >20% were obtained within 24 h, yielding rapidly decelerating creep (cf. Figure 5) and microstructures dominated by closed ring-type structures (see Figure 8c).

[46] Again, this behavior is consistent with expectations as the $4\gamma/d$ term becomes progressively more significant compared with $a\sigma_{\text{eff}}/e_v$ in equations (9) and (10). Overall, however, noting the inverse cubic dependence of strain rate on grain size seen at the coarser grain sizes, it is evident that the behavior observed in the high-stress regime is best explained by the diffusion controlled model of equation (9), along with the existence of a finite yield stress, equal to $4\gamma/d$. This yield stress must be exceeded for densification by stress-driven pressure solution to occur. As the term $a\sigma_{\text{eff}}/e_v$ falls to values approaching $4\gamma/d$ during compaction, compaction decelerates rapidly as the driving force for pressure solution falls to zero. When $4\gamma/d > a\sigma_{\text{eff}}/e_v$, mass is ultimately transferred from pore walls to grain contacts, or neck growth at contact margins becomes significant.

5.2. The High-Stress Regime: Grain Boundary Diffusivity

[47] From the above it is inferred that between 10 to 25% compaction, in the regime $d > 20$ μm and $\sigma_{\text{eff}} > 0.025$ MPa, deformation of wet NaNO$_3$ aggregates occurs by grain boundary diffusion-controlled pressure solution creep as described by equation (9), with no significant retarding effect due to the interfacial energy driving forces. However, at higher strains and longer times, our data imply that contact healing and/or neck growth and grain growth processes become dominant, pulling the system toward equilibrium, and leading to more complicated mechanical behavior.

[48] For diffusion-controlled pressure solution creep with negligible influence of interfacial energy effects, as seen in our experiments at $d > 20$ μm, $\sigma_{\text{eff}} > 0.025$ MPa and $e_v = 10–25\%$, it is possible to obtain an estimate of the effective grain boundary diffusivity product, $Z^* = D_{\text{gb}}CS$. A best fit to equation (9) was calculated based on experimental strain rate data, taking $4\gamma/d = 0$. Data obtained for various grain size batches (i.e., $d = 25, 39, 63, 104$ and 250 μm), at applied stresses of 0.3 MPa, 1 MPa and 4.9 MPa and volumetric strains of 10% and 20% were used. The values obtained for the grain boundary diffusivity product Z^* lie in the range $5.7 \pm 4 \cdot 10^{-20}$ m^3/s. This agrees well with values in the range of $10^{-19}–10^{-20}$ m^3/s obtained for pressure solution creep in other salts and minerals [*de Meer et al.*, 2002; *Spiers et al.*, 1990; *Spiers and Brzesowsky*, 1993; *Spiers et al.*, 2004; *van Noort et al.*, 2011; *Zhang et al.*, 2010]. Though the present Z^* values showed no dependence on stress or grain size in the range calculated, Z^* was

found to be up to a factor two smaller at 20% volumetric strain than at 10%. This could be the result of changes in the grain boundary thickness, island population or channel tortuosity during the experiments. The active grain boundary thickness $S = \delta (1 - \alpha)$, where δ is the grain boundary width and α the fraction of islands, is difficult to establish from microstructural observations after densification. Some separated contacts show surface roughness on the scale of a few hundred nm, suggesting an island-channel structure with the grain-to-grain contacts. However, larger and smaller amplitude roughness also was observed. Therefore, further analysis of the diffusivity product Z^* to constrain the diffusion coefficient in the grain boundary fluid is not attempted.

5.3. The Low-Stress Regime

[49] At low stresses, that is, $\sigma_{eff} < 0.025$ MPa, and grain sizes of <20 μm, the observed compaction behavior shows anomalously low-strain rates compared to the high-stress behavior, with the apparent stress exponent n rapidly increasing toward low stresses (see Figures 6c and 6d versus Figures 6a and 6b). Moreover, a strongly positive grain size dependence of the strain rate was observed, instead of the inverse dependence observed for pressure solution creep in the high-stress regime (Figure 7). In addition, it should be noted that the low-stress experiments became immeasurably slow beyond strains of ~20%. This type of behavior is consistent with that predicted by the extended pressure solution model (equation (9)) when the interfacial energy term ($4\gamma/d$) becomes equal to the stress term ($a\sigma_{eff}/e_v$). The relative magnitude of the interfacial energy term calculated, using $\gamma \approx 0.27$ J/m^2 [Dzerhakhov et al., 1986] and $3/(\pi\sqrt{2})$ for the geometrical term a, based on an FCC packing, shows that interfacial energy cannot be neglected in the low-stress experiments, especially when d is small. On the other hand, neck- or grain-growth processes could also be partially responsible for the anomalously low creep rates seen at low stress and fine grain size, as the rate of these independent processes becomes (locally) more significant compared to pressure solution. The microstructures observed in the low-stress samples provide some evidence for active pressure solution. However, most samples show ring-type neck structures at grain contacts, both closed and partially open (Figures 8c and 8f). Furthermore, grain growth (Figure 8h) was observed, as well as a change of grain shape, from subspherical to euhedral (faceted) at effective stresses of less than 0.005 MPa (Figure 8g). These samples attained only very low strains (<10%). The observed grain growth and grain shape changes move the microstructure closer to equilibrium, from a high to low interfacial energy configuration. This implies an important interfacial free energy contribution to mass transfer, as well as an important influence of interfacial energy anisotropy on the microstructure.

6. Synthesis and Implications

[50] From the experiments, it has become evident that pressure solution compaction rates increase with decreasing grain size, as established in previous studies [de Meer and Spiers, 1997; Zhang and Spiers, 2005]. However, there is a lower limit beyond which compaction rates decrease with decreasing stress, decreasing grain size and increasing compaction strain, as a result of interfacial energy driving

forces that oppose pressure solution (stress-related driving forces). The behavior observed in the present NaNO$_3$ analog material is well explained by the model for the competing effects of stress and interfacial energy driving forces that were derived (equation (9)), at least in qualitative terms. Neck and grain growth processes may have played a role in inhibiting pressure solution in the finer-grained samples at low stress. Local variations in stress, grain size and surface curvature, and anisotropy effects may have created a more gradual transition to interfacial energy dominance than predicted by the model. Broadly though, the extended model for diffusion-controlled pressure solution including interfacial energy (equation (9)) seems to apply for NaNO$_3$. Therefore, it can be expected that the effects of interfacial energy embodied in equations (9) and (10) will influence pressure solution compaction of other geological materials, regardless of rate-controlling mechanisms.

[51] The present results may have significant implications for making predictions of pressure solution healing, sealing and strength recovery in very fine-grained materials, such as fault gouges in both major fault systems [Jefferies et al., 2006; Wibberley and Shimamoto, 2003] and in faults sealing hydrocarbon reservoirs [Fisher and Knipe, 1998]. Rates of compaction [Niemeijer et al., 2010], healing/sealing [Keulen et al., 2008; Niemeijer et al., 2008] and restrengthening [Tenthorey et al., 2003; Yasuhara et al., 2005] of active fault systems may be overestimated if pressure solution rates are extrapolated to very fine grain sizes. In turn, this may lead to underestimates of the repeat frequency of seismogenic activity in such fault zones, as well as to underestimates of their permeability. As a first estimate of the grain size at which such effects might become important in quartz-rich fault gouge, the term ($a\sigma_{eff}/e_v - 4\gamma/d$) = 0 is rearranged to yield $d = 4\gamma e_v/a\sigma_{eff}$. Inserting $a = 3/(\pi\sqrt{2})$, $\sigma_{eff} = 25$–125 MPa (2–10 km depth, lithostatic gradient = 22.7 MPa/km, pore pressure gradient = 10 MPa/km), porosity $\varphi = 10\%$ (equivalent to $e_v = (\varphi_0 - \varphi)/(1 - \varphi) = 30\%$ for $\varphi_0 = 35\%$) and $\gamma_{quartz} = 0.145$ J/m^2 [Hiraga et al., 2002], as appropriate for mid-upper crustal (seismogenic) depths, suggests that the grain size d should be of the order of ~10 nm for interfacial energy effects to become significant (yield stress of $4\gamma/d \approx 56$ MPa). This would mean that ultrafine nanogouge ($d \leq 10$ nm) may not compact and cement by pressure solution. However, gouges with coarser grain size would be expected to undergo pressure solution. Conversely, a gouge matrix grain size of 1–10 μm would imply a minimum effective stress to activate pressure solution (yield stress) of only ~25–250 kPa. Finally, it should be noted that while strong evidence has been presented here for an inhibiting effect of interfacial energy driving forced on pressure solution creep, the detailed mechanism underlying the observed contact healing features and grain size-dependent yield stress remains to be identified. A consideration of the stability of closed rim structures (including necks as well as ring islands) against undercutting or finger-like penetration from outside may elucidate this in the future.

7. Conclusions

[52] An extended pressure solution model was derived to include the effects of surface energy during compaction of

granular materials. Uniaxial compaction creep experiments were performed on fine-grained (8–250 μm) $NaNO_3$ aggregates to test the applicability of this model to a material showing pressure solution at room temperature and pressure. The main findings and conclusions are as follows.

[53] 1. Dry and oil saturated material showed no significant creep. However, rapid creep occurred in the presence of $NaNO_3$-saturated solution. This was primarily due to pressure solution.

[54] 2. At volumetric strains of 10–20%, $d > 20$ μm and $\sigma_{\mathrm{eff}} > 0.025$ MPa, the wet compacted $NaNO_3$ aggregates showed a dependence of compaction rates on stress, grain size and volumetric strain, that is, $\dot{\varepsilon} \propto \dfrac{\sigma^{\sim 1}}{d^3 e_v^{2-5}}$. This is roughly consistent with a pressure solution creep model for the case of grain boundary diffusion control when interfacial energy effects are negligible, that is, with conventional models for diffusion-controlled pressure solution.

[55] 3. For grain sizes smaller than 20 μm, we observed unusual mechanical behavior. The rate of densification decreased with decreasing grain size. For experiments with $\sigma_{\mathrm{eff}} < 0.025$ MPa, a rapid increase in the stress sensitivity of strain rate was observed toward lower stresses. Order of magnitude calculations indicate that the interfacial energy effect on pressure solution creep cannot be neglected under these conditions.

[56] 4. Microstructural analysis of the wet samples showed evidence for pressure solution creep features, such as indentations, truncations and overgrowths, but also showed neck growth and grain growth, suggesting an approach to microstructural equilibrium at longer compaction times, that is, after the initial relatively rapid deformation of 20–30%. Distinct differences in microstructure were observed between samples compacted at high stress (>0.025 MPa) and low volumetric strains (<20%), which showed pressure solution features, versus those compacted at low stress (<0.025 MPa) or at high effective stress at high volumetric strain (>20%), which showed neck and grain growth features.

[57] 5. It is inferred that the initial rapid densification of the wet $NaNO_3$ aggregates occurred by stress-driven, grain boundary diffusion-controlled pressure solution creep, while interfacial energy-related grain-contact, grain-neck and grain-growth processes dominated at low stresses, small grain sizes and at larger strains. Estimation of $Z^* = D_{gb}CS$, the effective grain boundary diffusivity product associated with grain boundary diffusion-controlled pressure solution creep, gives a value of $5.7 \pm 4 \cdot 10^{-20}$ m^3/s, in the high-stress regime where $d > 20$ μm, $\sigma_{\mathrm{eff}} > 0.3$ MPa, $e_v > 10\%$, which is in reasonably good agreement with values reported in the literature for other highly soluble salts.

[58] 6. At low applied stresses ($\sigma_{\mathrm{eff}} < 0.025$ MPa) and fine grain sizes (<20 μm), the microstructures and rapidly decelerating strain rates observed indicate that interfacial energy-related driving forces become significant. The results demonstrate a yield stress effect that is broadly consistent with the predictions of the extended pressure solution densification model, for the case when the interfacial energy term ($4\gamma/d$) approaches the stress term ($a\sigma_{\mathrm{eff}}/e_v$). This has implications for the prediction of compaction and healing/sealing rates for very fine-grained materials, such as fault

gouges in seismogenic fault systems. For materials such as quartz nanogouge with a grain size of $\sim$10 nm, pressure solution compaction is expected to be strongly inhibited, exhibiting a yield stress of $\sim$25–125 MPa. For grain sizes of about 1–10 μm, the new model implies a yield stress for pressure solution of 25–250 kPa. However, the details of the mechanism controlling contact healing and the observed, grain size-dependent yield stress remain to be elucidated.

References

Bos, B., and C. J. Spiers (2001), Experimental investigation into the microstructural and mechanical evolution of phyllosilicate-bearing fault rock under conditions favouring pressure solution, *J. Struct. Geol.*, *23*(8), 1187–1202, doi:10.1016/S0191-8141(00)00184-X.

Bos, B., and C. J. Spiers (2002), Fluid-assisted healing processes in gouge-bearing faults: Insights from experiments on a rock analogue system, *Pure Appl. Geophys.*, *159*, 2537–2566, doi:10.1007/s00024-002-8747-2.

Bulau, J. R., H. S. Waff, and J. A. Tyburczy (1979), Mechanical and thermodynamic constraints on fluid distribution in partial melts, *J. Geophys. Res.*, *84*(B11), 6102–6108, doi:10.1029/JB084iB11p06102.

Coble, R. L. (1967), Mechanisms of densification during hot pressing, in *Sintering and Related Phenomena*, edited by G. C. Kuczynski et al., pp. 329–350, Gordon and Breach, New York.

Coble, R. L. (1970), Diffusion models for hot pressing with surface energy and pressure effects as driving forces, *J. Appl. Phys.*, *41*, 4798, doi:10.1063/1.1658543.

de Meer, S., and C. J. Spiers (1995), Creep of wet gypsum aggregates under hydrostatic loading conditions, *Tectonophysics*, *245*, 171–183, doi:10.1016/0040-1951(94)00233-Y.

de Meer, S., and C. J. Spiers (1997), Uniaxial compaction of wet gypsum aggregates, *J. Geophys. Res.*, *102*, 875–891, doi:10.1029/96JB02481.

de Meer, S., et al. (2002), Diffusive properties of fluid-filled grain boundaries measured electrically during active pressure solution, *Earth Planet. Sci. Lett.*, *200*(1–2), 147–157, doi:10.1016/S0012-821X(02)00585-X.

den Brok, B., et al. (1999), Pressure solution compaction of sodium chlorate and implications for pressure solution in NaCl, *Tectonophysics*, *307*(3–4), 297–312, doi:10.1016/S0040-1951(99)00103-1.

Dewhurst, D. N., and R. M. Jones (2002), Geomechanical, microstructural, and petrophysical evolution in experimentally reactivated cataclasites: Applications to fault seal prediction, *AAPG Bull.*, *86*(8), 1383–1405.

Dzerhakhov, N., et al. (1986), Determination of surface energies of carbonates with a calcite structure, *God. Vissh. Minno-Geol. Inst., Sofiya*, *31*, 201–206.

Elsworth, D., and H. Yasuhara (2006), Short-timescale chemo-mechanical effects and their influence on the transport properties of fractured rock, *Pure Appl. Geophys.*, *163*, 2051–2070, doi:10.1007/s00024-006-0113-3.

Evans, B. E., et al. (2001), A few remarks on the kinetics of static grain growth in rocks, *Int. J. Earth Sci.*, *90*(1), 88–103, doi:10.1007/s005310000150.

Faul, U. H. (1997), Permeability of partially molten upper mantle rocks from experiments and percolation theory, *J. Geophys. Res.*, *102*(B5), 10,299–10,311, doi:10.1029/96JB03460.

Fisher, Q. J., and R. J. Knipe (1998), Fault sealing processes in siliciclastic sediments, in *Faulting, Fault Sealing and Fluid Flow in Hydrocarbon Reservoirs*, edited by G. Jones, Q. J. Fisher, and R. J. Knipe, *Geol. Soc. Spec. Publ.*, *147*, 117–134, doi:10.1144/GSL.SP.1998.147.01.08.

German, R. M. (1985), *Liquid Phase Sintering*, Plenum, New York.

Gibbs, J. W. (1878), On the equilibrium of heterogeneous substances, *Trans. Conn. Acad. Arts Sci.*, *3*, 343–524.

Gratier, J.-P., R. Guiguet, F. Renard, L. Jenatton, and D. Bernard (2009), A pressure solution creep law for quartz from indentation experiments, *J. Geophys. Res.*, *114*, B03403, doi:10.1029/2008JB005652.

Green, H. W., II (1984), "Pressure solution" creep: Some causes and mechanisms, *J. Geophys. Res.*, *89*(B6), 4313–4318, doi:10.1029/JB089iB06p04313.

Gundersen, E., F. Renard, D. K. Dysthe, K. Bjørlykke, and B. Jamtveit (2002), Coupling between pressure solution creep and diffusive mass transport in porous rocks, *J. Geophys. Res.*, *107*(B11), 2317, doi:10.1029/2001JB000287.

Hay, R. S., and B. Evans (1988), Intergranular distribution of pore fluid and the nature of high angle grain boundaries in limestone and marble, *J. Geophys. Res.*, *93*(B8), 8959–8974, doi:10.1029/JB093iB08p08959.

Heidug, W. K. (1991), A thermodynamic analysis of the conditions of equilibrium at non-hydrostatically stressed and curved solid-fluid interfaces, *J. Geophys. Res.*, *96*(B13), 21,909–21,921, doi:10.1029/91JB02173.

Hickman, S. H., and B. Evans (1991), Experimental pressure solution in halite: The effect of grain/interphase boundary structure, *J. Geol. Soc.*, *148*, 549–560, doi:10.1144/gsjgs.148.3.0549.

Hiraga, T., et al. (2002), Interfacial energies for quartz and albite in pelitic schist, *Contrib. Mineral. Petrol.*, *143*(6), 664–672, doi:10.1007/s00410-002-0375-4.

Jefferies, S. P., et al. (2006), Origin and mechanical significance of foliated cataclastic rocks in the cores of crustal-scale faults: Examples from the Median Tectonic Line, Japan, *J. Geophys. Res.*, *111*, B12303, doi:10.1029/2005JB004205.

Jurewicz, S. R., and E. B. Watson (1985), The distribution of a partial melt in a granitic system: The application of liquid sintering theory, *Geochim. Cosmochim. Acta*, *49*, 1109–1121, doi:10.1016/0016-7037(85)90002-X.

Keulen, N., H. Stünitz, and R. Heilbronner (2008), Healing microstructures of experimental and natural fault gouge, *J. Geophys. Res.*, *113*, B06205, doi:10.1029/2007JB005039.

Koelemeijer, P. J., C. J. Peach, and C. J. Spiers (2012), Surface diffusivity of cleaved NaCl crystals as a function of humidity: Impedance spectroscopy measurements and implications for crack healing in rock salt, *J. Geophys. Res.*, *117*, B01205, doi:10.1029/2011JB008627.

Lehner, F. K. (1990), Thermodynamics of rock deformation by pressure solution, in *Deformation Processes in Minerals Ceramics and Rocks*, edited by D. J. Barber and P. G. Meredith, pp. 296–333, Unwin Hyman, London.

Lehner, F. K. (1995), A model for intergranular pressure solution in open systems, *Tectonophysics*, *246*, 153–170, doi:10.1016/0040-1951(94)00232-X.

Lehner, F. K., and J. Bataille (1984), Non-equilibrium thermodynamics of pressure solution, *Pure Appl. Geophys.*, *122*, 53–85, doi:10.1007/BF00879649.

Morrow, C. A., and J. D. Byerlee (1989), Experimental studies of compaction and dilatancy during frictional sliding on faults containing gouge, *J. Struct. Geol.*, *11*(7), 815–825, doi:10.1016/0191-8141(89)90100-4.

Niemeijer, A. R., et al. (2002), Compaction creep of quartz sand at 400–600°C: Experimental evidence for dissolution-controlled pressure solution, *Earth Planet. Sci. Lett.*, *195*(3–4), 261–275, doi:10.1016/S0012-821X(01)00593-3.

Niemeijer, A., C. Marone, and D. Elsworth (2008), Healing of simulated fault gouges aided by pressure solution: Results from rock analogue experiments, *J. Geophys. Res.*, *113*, B04204, doi:10.1029/2007JB005376.

Niemeijer, A., C. Marone, and D. Elsworth (2010), Frictional strength and strain weakening in simulated fault gouge: Competition between geometrical weakening and chemical strengthening, *J. Geophys. Res.*, *115*, B10207, doi:10.1029/2009JB000838.

Olgaard, D. L., and B. Evans (1988), Grain growth in synthetic marbles with added mica and water, *Contrib. Mineral. Petrol.*, *100*(2), 246–260, doi:10.1007/BF00373591.

Pharr, G. M., and M. F. Ashby (1983), On creep enhanced by a liquid phase, *Acta Metall.*, *31*, 129–138, doi:10.1016/0001-6160(83)90072-X.

Raj, R. (1982), Creep in polycrystalline aggregates by matter transport through a liquid phase, *J. Geophys. Res.*, *87*(B6), 4731–4739, doi:10.1029/JB087iB06p04731.

Raj, R., and C. K. Chyung (1981), Solution-precipitation creep in glass ceramics, *Acta Metall.*, *29*, 159–166, doi:10.1016/0001-6160(81)90096-1.

Ravikiran, J. (1995), Effect of speed and pressure on dry sliding interactions of alumina against steel, *J. Am. Ceram. Soc.*, *78*(2), 356–364, doi:10.1111/j.1151-2916.1995.tb08808.x.

Renard, F., et al. (1999), An integrated model for transitional pressure solution in sandstones, *Tectonophysics*, *312*, 97–115, doi:10.1016/S0040-1951(99)00202-4.

Revil, A. (2001), Pervasive pressure solution transfer in a quartz sand, *J. Geophys. Res.*, *106*(B5), 8665–8686, doi:10.1029/2000JB900465.

Revil, A., P. Leroy, A. Ghorbani, N. Florsch, and A. R. Niemeijer (2006), Compaction of quartz sands by pressure solution using a Cole-Cole distribution of relaxation times, *J. Geophys. Res.*, *111*, B09205, doi:10.1029/2005JB004151.

Robin, P. Y. F. (1978), Pressure solution at grain contacts, *Geochim. Cosmochim. Acta*, *42*, 1383–1389, doi:10.1016/0016-7037(78)90043-1.

Rutter, E. H. (1976), The kinetics of rock deformation by pressure solution, *Philos. Trans. R. Soc. London, Ser. A*, *283*, 203–219, doi:10.1098/rsta.1976.0079.

Spiers, C. J., and R. H. Brzesowsky (1993), Densification behaviour of wet granular salt: Theory versus experiment, in *Seventh Symposium on Salt*, vol. 1, edited by H. Kakihana et al., pp. 83–92, Elsevier Sci., Amsterdam.

Spiers, C. J., and P. M. T. M. Schutjens (1990), Densification of crystalline aggregates by fluid phase diffusional creep, in *Deformation Processes in Minerals, Ceramics and Rocks*, edited by D. J. Barber and P. G. Meredith, pp. 334–353, Unwin Hyman, London.

Spiers, C. J., and P. M. T. M. Schutjens (1999), Intergranular pressure solution in NaCl: Grain-to-grain contact experiments under the optical microscope, *Oil Gas Sci. Technol.*, *54*(6), 729–750.

Spiers, C. J. et al. (1990), Experimental determination of constitutive parameters governing creep of rocksalt by pressure solution, in *Deformation Mechanisms, Rheology and Tectonics*, edited by R. J. Knipe and E. H. Rutter, *Geol. Soc. Spec. Publ.*, *54*, 215–227, doi:10.1144/GSL.SP.1990.054.01.21.

Spiers, C. J. et al. (2004), Kinetics of rock deformation by pressure solution and the role of thin aqueous films, in *Physicochemistry of Water in Geological and Biological Systems*, edited by S. Nakashima et al., pp. 129–158, Universal Acad. Press, Tokyo.

Tenthorey, E., et al. (2003), Evolution of strength recovery and permeability during fluid-rock reaction in experimental fault zones, *Earth Planet. Sci. Lett.*, *206*(1–2), 161–172, doi:10.1016/S0012-821X(02)01082-8.

van Noort, R., C. J. Spiers, and G. M. Pennock (2008a), Compaction of granular quartz under hydrothermal conditions: Controlling mechanisms and grain boundary processes, *J. Geophys. Res.*, *113*, B12206, doi:10.1029/2008JB005815.

van Noort, R., H. J. M. Visser, and C. J. Spiers (2008b), Influence of grain boundary structure on dissolution controlled pressure solution and retarding effects of grain boundary healing, *J. Geophys. Res.*, *113*, B03201, doi:10.1029/2007JB005223.

van Noort, R., et al. (2011), Structure and properties of loaded silica contacts during pressure solution: Impedance spectroscopy measurements under hydrothermal conditions, *Phys. Chem. Miner.*, *38*(7), 501–516, doi:10.1007/s00269-011-0423-6.

Visser, H. J. M. (1999), Mass transfer processes in crystalline aggregates containing a fluid phase, PhD thesis, Utrecht Univ., Utrecht, Netherlands.

Watanabe, T., and C. J. Peach (2002), Electrical impedance measurement of plastically deforming halite rocks at 125°C and 50 MPa, *J. Geophys. Res.*, *107*(B1), 2004, doi:10.1029/2001JB000204.

Watson, E. B., and J. M. Brenan (1987), Fluids in the lithosphere 1. Experimentally determined wetting characteristics of CO_2-H_2O fluids and the implications for fluid transport, host-rock physical properties and fluid inclusions formation, *Earth Planet. Sci. Lett.*, *85*, 497–515, doi:10.1016/0012-821X(87)90144-0.

Wibberley, C. A. J., and T. Shimamoto (2003), Internal structure and permeability of major strike-slip fault zones: The median tectonic line in Mie prefecture, southwest Japan, *J. Struct. Geol.*, *25*(1), 59–78, doi:10.1016/S0191-8141(02)00014-7.

Yasuhara, H., C. Marone, and D. Elsworth (2005), Fault zone restrengthening and frictional healing: The role of pressure solution, *J. Geophys. Res.*, *110*, B06310, doi:10.1029/2004JB003327.

Zhang, X., and C. J. Spiers (2005), Compaction of granular calcite by pressure solution at room temperature and effects of pore fluid chemistry, *Int. J. Rock Mech. Min. Sci.*, *42*, 950–960, doi:10.1016/j.ijrmms.2005.05.017.

Zhang, X. et al. (2002), Compaction experiments on wet calcite powder at room temperature: Evidence for operation of intergranular pressure solution, in *Deformation Mechanisms, Rheology and Tectonics: Current Status and Future Perspectives*, edited by S. De Meer et al., *Geol. Soc. Spec. Publ.*, *200*, 29–39, doi:10.1144/GSL.SP.2001.200.01.02.

Zhang, X., C. J. Spiers, and C. J. Peach (2010), Compaction creep of wet granular calcite by pressure solution at 28°C to 150°C, *J. Geophys. Res.*, *115*, B09217, doi:10.1029/2008JB005853.